Q. J. R. Meteorol. Soc. (2004), **130**, pp. 1075–1102 doi: 10.1256/qj.03.72

Polar low *le Cygne*: Satellite observations and numerical simulations

By CHANTAL CLAUD[1]*, GUENTHER HEINEMANN[2], ELMER RAUSTEIN[3] and LYNN MCMURDIE[4]

[1]*Laboratoire de Météorologie Dynamique/IPSL, Ecole Polytechnique, Palaiseau, France*
[2]*Meteorologisches Institut Universität Bonn, Germany*
[3]*Department of Meteorology, Geophysical Institute, University of Bergen, Norway*
[4]*Department of Atmospheric Sciences, University of Washington, Seattle, USA*

(Received 23 April 2003; revised 13 October 2003)

SUMMARY

A polar low (PL) which occurred in October 1993 over the Norwegian Sea is investigated from an observational and a numerical point of view. This PL has several unique features: it developed early in the season, it lasted for about 3 days, and its trajectory was such that it passed over weather stations so that 'conventional' observations of the low are available. The conditions of the formation, development and decay of the PL are investigated using a double approach: satellite data from several instruments are used together to document the mesoscale structure of the low, and two versions of a limited-area model are run to investigate the dynamics of the low. Numerical model fields are compared to quantities derived from TIROS-N Operational Vertical Sounder, the Special Sensor Microwave/Imager, and satellite radar altimeter data. In spite of a better spatial resolution of the models, humidity and surface wind speeds are less organized in the simulations than in satellite retrievals. The number of vertical levels, especially for the lowest layers of the atmosphere, appears to be an essential component for a good simulation of the trajectory of the low. There is, however, good overall agreement between modelled and satellite-derived fields, and the good quality of the simulations allows inferences to be made regarding the essential physical and dynamical processes taking place during the formation and development of the PL. We find that the PL was the result of favourable flow conditions at the surface in the form of a shallow arctic front established south of the ice edge, together with an upper-level potential-vorticity anomaly setting the stage for a positive interaction. Later on, the strong surface sensible- and latent-heat fluxes contributed to the extensive vertical development. This study demonstrates the usefulness of the approach adopted here, which relies not only on simulations but also on observations to get a very complete description of such disturbances.

KEYWORDS: Polar-low life cycle PV anomaly

1. INTRODUCTION

Polar lows (PLs) are mesoscale cyclones that form over open sea during the cold season within polar air masses. Several PLs developing over Arctic oceans have been extensively studied during the last two decades. Although operational numerical weather prediction models have horizontal and vertical resolutions capable of simulating these phenomena in some detail, PLs still represent a major problem for operational weather forecasting due to their occurrence in remote areas and their characteristics (short-lived and small-scale but extremely active weather phenomena). The Norwegian Sea (NWS), with a relatively good coverage of conventional observations, represents one of the best areas for the study of Arctic PLs. Previous studies for this region lead to the conclusion that baroclinic instability associated with upper-level cold air advection and cold air masses over relatively warm water seems to be the dominating mechanism for most PLs (see Grønås *et al.* 1987; Nordeng and Rasmussen 1992; Nielsen 1997, hereafter N97). However, the importance of Conditional Instability of the Second Kind, and Air–Sea Interaction Instability (Emanuel 1986; Emanuel and Rotunno 1989) now called Wind Induced Surface Heat Exchange, was also noted for a few cases (e.g. Rasmussen 1989). In the western part of the NWS the orographic structures of Greenland can also play a role in the cyclogenesis of PLs (Klein and Heinemann 2002).

The current paper investigates a PL case called *le Cygne* (the swan, after its shape on satellite imagery (see Fig. 1(b)) which formed early on 14 October 1993 at around

* Corresponding author: Laboratoire de Météorologie Dynamique/IPSL, Ecole Polytechnique, Palaiseau, France.
e-mail: chclaud@lmd.polytechnique.fr

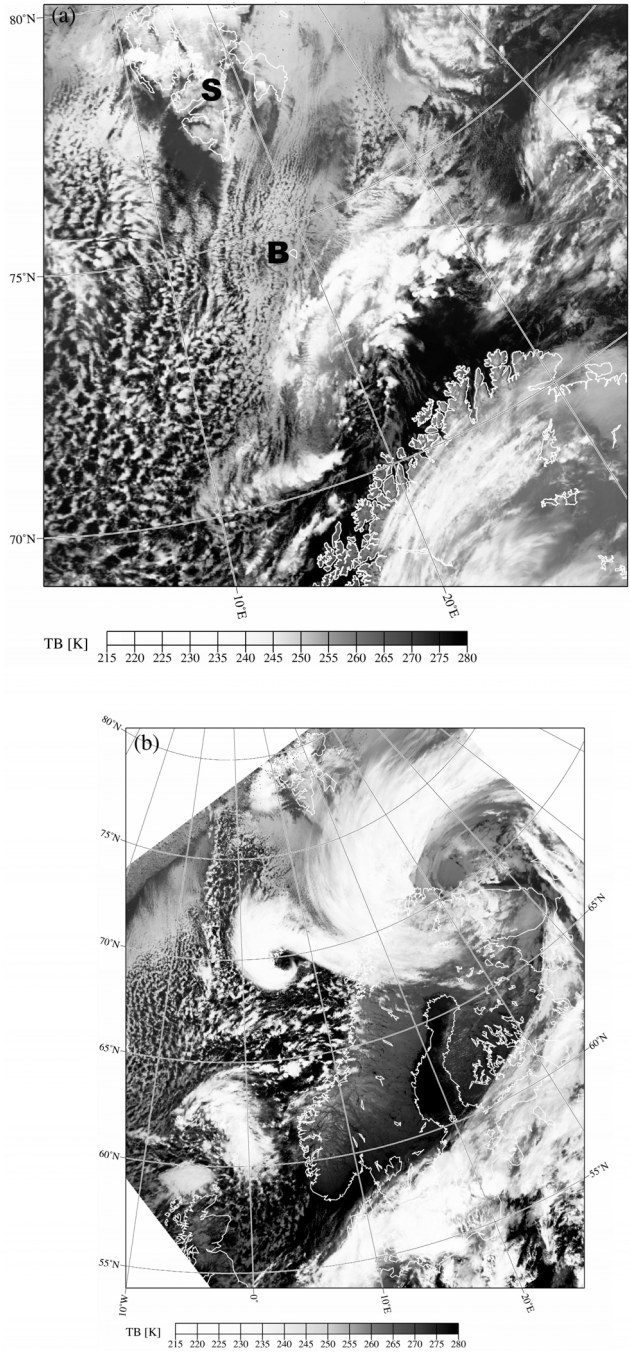

Figure 1. NOAA/AVHRR (see text) channel 4 brightness temperatures (K) for: (a) 0357 UTC 13 October, (b) 1341 UTC 14 October, (c) 1329 UTC 15 October, and (d) 0504 UTC 16 October 1993. Bear Island and Spitzbergen are marked in (a) as B and S, respectively.

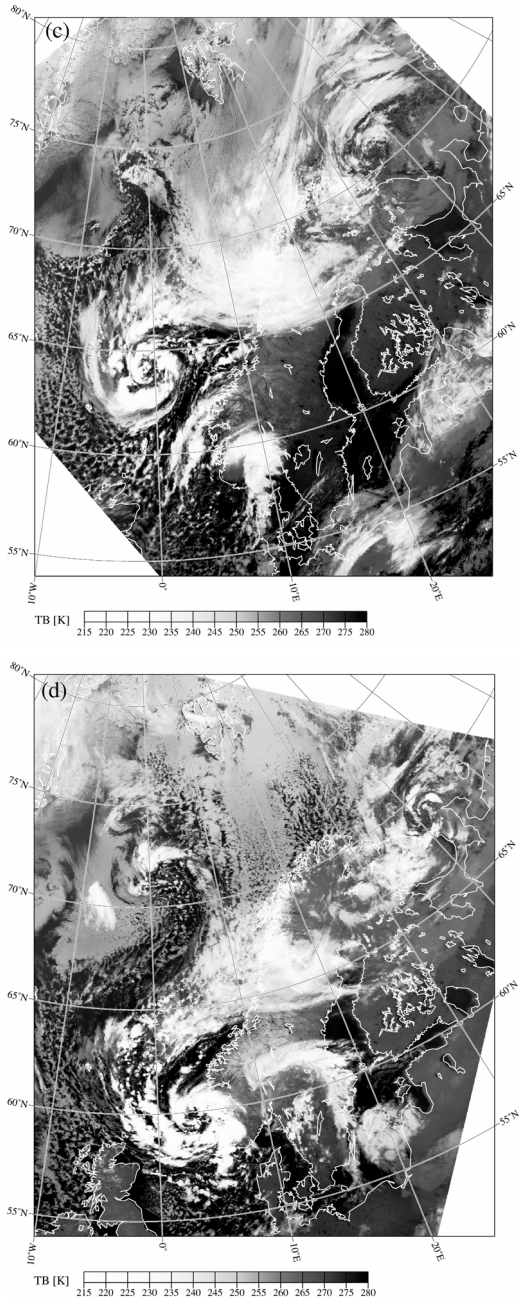

Figure 1. Continued.

72°N, 5–10°E, to the rear of a synoptic-scale cyclone. The PL moved southwards almost parallel to the Norwegian coast with a speed of about 10 m s^{-1}, before decaying over southern Norway on 16 October. Significant changes in cloud structure occurred during its lifetime with evolution from a so-called 'comma-cloud' to a spiraliform PL, suggesting that during the growth of the PL the ongoing mechanisms changed.

Several studies have demonstrated the potential of satellite retrievals for PL studies (Claud *et al.* 1993; Carleton *et al.* 1995; Heinemann 1996; Rasmussen *et al.* 1996; McMurdie *et al.* 1997). In this study, a combination of the following three sensors is used: the TIROS-N Operational Vertical Sounder (TOVS), the Special Sensor Microwave/Imager (SSM/I) of the Defense Meteorological Satellite Program (DMSP) and the Topex/Poseidon radar altimeter. Since these do not fly on the same spacecraft, one can take advantage of the different sampling times and areas.

Mesoscale limited-area models with horizontal resolutions similar to the resolution of the satellite sensors described above have been used successfully for numerical simulation of several PLs (e.g. Nordeng 1990; Nordeng and Rasmussen 1992). The particular PL discussed in this paper was previously simulated using the High-Resolution Limited Area Model by N97. The main conclusion of that work was that this low initially formed by baroclinic instability along a frontal zone within a maritime polar air mass, and that latent-heat fluxes were necessary for the PL formation. One of the conclusions of N97 was that it is desirable to consider satellite data in order to get detailed information about the three-dimensional dynamic and thermodynamic structure of the PL, and to compare them with model simulations. The present study, indeed, gives new insights into this PL development through a multi-sensor satellite data investigation and its simulation by two versions of a mesoscale model. The model is the Norwegian Limited Area model (NORLAM) developed at the Norwegian Meteorological Institute (Grønås *et al.* 1987). In contrast to N97, we focus on the genesis stage of the PL, and started simulations 12 h earlier. While N97 analysed the PL development using quasi-geostrophic theory, we use the isentropic potential vorticity (IPV) theory in the current paper.

Satellite-based studies provide information about the three-dimensional structure of the PL, but they cannot alone explain development mechanisms. On the other hand, model-based studies often lack a validation by observational data. In this study, satellite imagery and retrievals are used to provide a description of the PL, but they also serve to validate the model simulations by enabling comparison with satellite-retrieved fields.

The data and retrieval algorithms as well as the models are described in section 2. In section 3 the synoptic situation is described, using AVHRR (Advanced Very High-Resolution Radiometer) imagery together with surface and upper-level analyses. In section 4, the evolution of the low is examined through the investigation of satellite-derived temperature and moisture structure, along with cloud parameters, surface wind speed and sea state. Three phases are distinguished based on satellite imagery: the incipient stage, the developed (or mature) stage, and the decaying stage. Section 5 follows with the major results of the numerical simulations. In section 6, comparisons between the models themselves, and between models and satellite retrievals, are presented. Finally, in the last section results are summarized and the mechanisms involved in this development are discussed.

2. Satellite data and numerical models

(*a*) *Data and retrieval algorithms*

In this study, observations from different sensors, namely a vertical sounder, a microwave passive sensor and a microwave active sensor have been used. Data from

an imager complemented these observations. At the time of *le Cygne*, the ERS-1 satellite carrying the first satellite-borne C-band scatterometer was already launched. Unfortunately, there were no good scatterometer data during the period of interest, ERS-1 being in radar mode rather than scatterometer mode.

(i) *AVHRR.* The imagery used in this study was provided by the AVHRR instrument which flies aboard NOAA satellites, together with the TOVS instrument (see (ii)). It is based on the radiance measurements in the infrared channel 4 (10.5–11.5 μm) and is available as High Resolution Picture Transmission data with a nadir resolution of 1.1 km. Only NOAA11 data are used, which yield an overpass over the NWS every 12 h (at approximately 05 and 14 UTC).

(ii) *TOVS.* For investigating the atmospheric environment of the PL in terms of temperature, TOVS observations have been used. The TOVS consists of three passive vertical sounding instruments (Smith *et al.* 1979): the High resolution Infrared Radiation Sounder (HIRS-2), a radiometer with 19 channels in the infrared band (from 3.7 to 15.0 μm) and one in the visible band (0.7 μm); the Microwave Sounding Unit (MSU), a microwave sounder with four channels in the vicinity of 55 GHz; and the Stratospheric Sounding Unit, a pressure-modulated infrared radiometer with three channels near 15 μm. Only HIRS-2 and MSU data have been used in this study.

The spatial resolution of the infrared sounder is about 17 km at nadir, whereas the spatial resolution of the microwave sounder is 100 km at nadir, with a swath width of about 2400 km. There are two operational satellites flying simultaneously; while a point at low latitudes is observed every 12 h, overlap between swaths at high latitudes allows more frequent sampling.

The spectral radiances measured by HIRS-2 and MSU are converted into atmospheric variables using the Improved Initialization Inversion (3I) algorithm (e.g. Chedin *et al.* 1985; Scott *et al.* 1999). The 3I horizontal resolution of 100 km $\times$ 100 km (3I 'boxes') represents a compromise between the spatial resolution of HIRS-2 and MSU.

The 3I has been refined for use in polar and subpolar regions, in which temperature profiles up to 100 hPa have been found to compare well with radiosoundings provided thick enough layers are considered (Claud *et al.* 1991; Köpken *et al.* 1995). Simulations of cold air pools by Heinemann *et al.* (1995) have shown that the horizontal minimum size for the detection of PLs using 3I retrievals is 200 km, without resorting to other data.

In addition to temperature profiles, another TOVS-derived parameter of interest for studying atmospheric systems is the so-called 'temperature of the lower stratosphere' (TLS). TLS represents the mean temperature of a layer situated just above the tropopause, and is generated through a combination of three HIRS-2 and two MSU channels. The degree of reliability of TLS for describing tropopause-level thermal structures and variations has been examined in detail for three intensive observing periods of FASTEX (the Fronts and Atlantic Storm-Track Experiment (Joly *et al.* 1997)) conducted over the northern Atlantic. It has been shown that TLS could be used for tracking upper-level precursors of surface lows (Fourrié *et al.* 2000). Global comparisons with synoptically based diagnostics (temperature on potential-vorticity (PV) surfaces, wind and geopotential height at 300 hPa) showed that TLS fields also allow the detection of upper-level structures such as troughs, ridges and tropopause breaks along the cyclonic-shear side of an upper-level jet.

(iii) *SSM/I.* This flies aboard satellites in the operational F-series of the DMSP. SSM/I is a passive radiometer, its operating frequencies are 19.35, 22.2, 37 and 85.5 GHz

in horizontal and vertical polarization, except for the 22.2 GHz channel which only operates in vertical polarization (Hollinger *et al.* 1987). The SSM/I has a 1380 km swath width, and the data resolution varies according to frequency: approximately 50 km for the 19 and 22.2 GHz channels, 30 km for the 37 GHz channel, and 15 km for the 85.5 GHz channel.

From the SSM/I brightness temperatures using linear combinations of several channels (Petty 1994a,b), fields of integrated water vapour (IWV), integrated cloud liquid-water content (ICLW), surface wind speed and scattering by large ice particles (S85) are generated over open water at a spatial resolution of 50 km. The IWV algorithm is regression-based using a linear combination of brightness temperatures measured by the 19, 22 and 37 GHz channels. A rms difference of 2.6 kg m^{-2} has been obtained when validating the algorithm against independent radiosondes. For wind speed, an adaptation of the algorithm developed by Goodberlet *et al.* (1989) has been used. It consists of a linear combination of brightness temperatures from the three lowest SSM/I frequencies. Under rain-free conditions, for winds in the range 3–25 m s^{-1}, a standard error of 2 m s^{-1} was found. The scattering-based solid-precipitation index, S85, relies on the following physical property: frozen precipitation-sized hydrometeors scatter high-frequency microwave emissions and produce a local 'cold spot' in the relatively high brightness temperature of raining clouds. High values of S85 (30–60) distributed in bands or discrete 'blobs' are a good indication of ice hydrometeors associated with convection. On the other hand, when the S85 index is low, i.e. 10–30, its interpretation is more ambiguous; such values can be generated by shallow convection or thick stratiform precipitating clouds. Finally, in the absence of significant precipitation, the ICLW can be obtained from a normalized polarization difference at 85 GHz (McMurdie *et al.* 1997).

Several previous studies for both hemispheres have shown the utility of such fields with a high level of accuracy for research into PLs (e.g. Claud *et al.* 1993; Carleton *et al.* 1995; Heinemann 1996; Rasmussen *et al.* 1996; McMurdie *et al.* 1997; Lieder and Heinemann 1999; Hewson *et al.* 2000).

(iv) *Topex–Poseidon Altimeter.* The Topex–Poseidon satellite altimeter is a short-pulse (3.125 ns) nadir-viewing radar altimeter operating at 13.6 GHz. The sea-state estimates derived from it and used in this analysis are: the wind speed deduced from the ocean backscatter measurements, and the significant wave height computed on board the satellite from the slope of the mean return waveform leading edge. Retrieved parameters are obtained at 10 km resolution. The algorithm applied to the ocean backscatter coefficient to infer wind speed, yields an accuracy of about 1.8 m s^{-1} (Witter and Chelton 1991).

(*b*) *An overview of the limited-area models*

The models used in this study are based on the Norwegian Limited Area model (NORLAM) developed at the Norwegian Meteorological Institute (DNMI; Grønås *et al.* 1987), which is a full physics hydrostatic primitive-equation model on a polar-stereographic map with the sigma-coordinate as the vertical reference frame.

The model version used at the University of Bonn is the NORLAM (version 9), which is run with a resolution of 97 by 121 horizontal grid points and 30 vertical sigma levels with the model top at 100 hPa. About half the levels are located below 850 hPa in order to resolve the boundary layer well. Runs with 25 km grid spacing are performed with lateral boundaries provided by 6-hourly European Centre for Medium-Range Weather Forecasts (ECMWF) analyses (with a spatial resolution of 1.125° latitude × 1.125° longitude for this study). The model domain is 2500 km by 3000 km

(corresponding to the area shown later in Fig. 2). A detailed description of the model set-up can be found in Heinemann (1998) and Klein and Heinemann (2002).

The model version used at the University of Bergen (NORLAMS) is basically the same as NORLAM, but in NORLAM cloud water is a diagnostic variable, whereas in NORLAMS it is treated as a prognostic variable, using the so-called Sundqvist scheme (Sundqvist *et al.* 1989) implemented in the model by Kvamstø (1992). The integration area and the number of horizontal grid points are the same as for the University of Bonn version 9; however, there are 18 sigma levels in the vertical with five levels below 850 hPa. For the initialization and 6-hourly boundary values, the same ECMWF analyses as described above are used.

3. Synoptic situation

Most PLs are believed to have a relatively short lifetime, less than 48 h (Businger and Reed 1989). *Le Cygne* represents an example of a PL with much greater longevity; from its genesis stage over the Barents Sea early on 14 October until its gradual decay above southern Norway late on 16 October it lasted roughly 72 h. The broad characteristics of the synoptic situation prior to the development of the PL, during its developing stage, and during its decaying stage are presented in the following.

(*a*) *Prior to its development and during the incipient stage*

During 13 and 14 October 1993, a synoptic-scale low pressure system was moving north-eastwards from southern Scandinavia towards the Kola Peninsula. Between this low and a high pressure system centred over Greenland, cold low-level winds from the north-north-east were blowing over the Barents Sea and NWS. The southward transport over increasing sea surface temperatures destabilized the air. The situation characterizing the genesis conditions for the PL is shown by the satellite image of 04 UTC 13 October (Fig. 1(a)). A cold air outbreak is indicated by the shallow cloud streets between Spitzbergen and Bear Island, and a cluster of high clouds is present to the south-east of the Bear Island. The large synoptic-scale low is lying over Sweden at about 63°N, 15°E at that time. During 13 October, its centre moves to the Kola peninsula's north-western coast, and its cloud mass dominates the southern Barents Sea. The satellite image at 14 UTC 13 October (not shown) indicates that the cloud cluster south-east of Bear Island has intensified and moved northwards by two degrees in connection with the large-scale circulation induced by the synoptic low. However, no signal of the incipient PL is identifiable, neither in the ECMWF analyses nor in the routine weather charts from DNMI (not shown). The first hint of the developing PL can be seen in the ECMWF analysis of 00 UTC 14 October (Fig. 2(a)), where a slight surface trough at around 73°N, 20°E extends between the Norwegian coast and Spitzbergen. A closed 500 hPa low is analysed south-west of the surface trough.

(*b*) *The development and decaying stages*

At 1341 UTC 14 October, the developing disturbance can be seen as a swan-like figure in the cloud fields in the NWS (Fig. 1(b)). At 12 UTC on this day the ECMWF analysis (Fig. 2(b)) shows a marked trough in the 1000 hPa contours in connection with the PL. From then on, it can be followed in the analyses until it decays in the afternoon of 16 October. The ECMWF analysis valid at 00 UTC 15 October (Fig. 2(c)) shows the PL as a pronounced trough moving southwards along the Norwegian coast, while the synoptic low has become stationary over the Kola Peninsula. On weather ship M (66°N, 2°E) a mesoscale disturbance passing southwards is clearly indicated

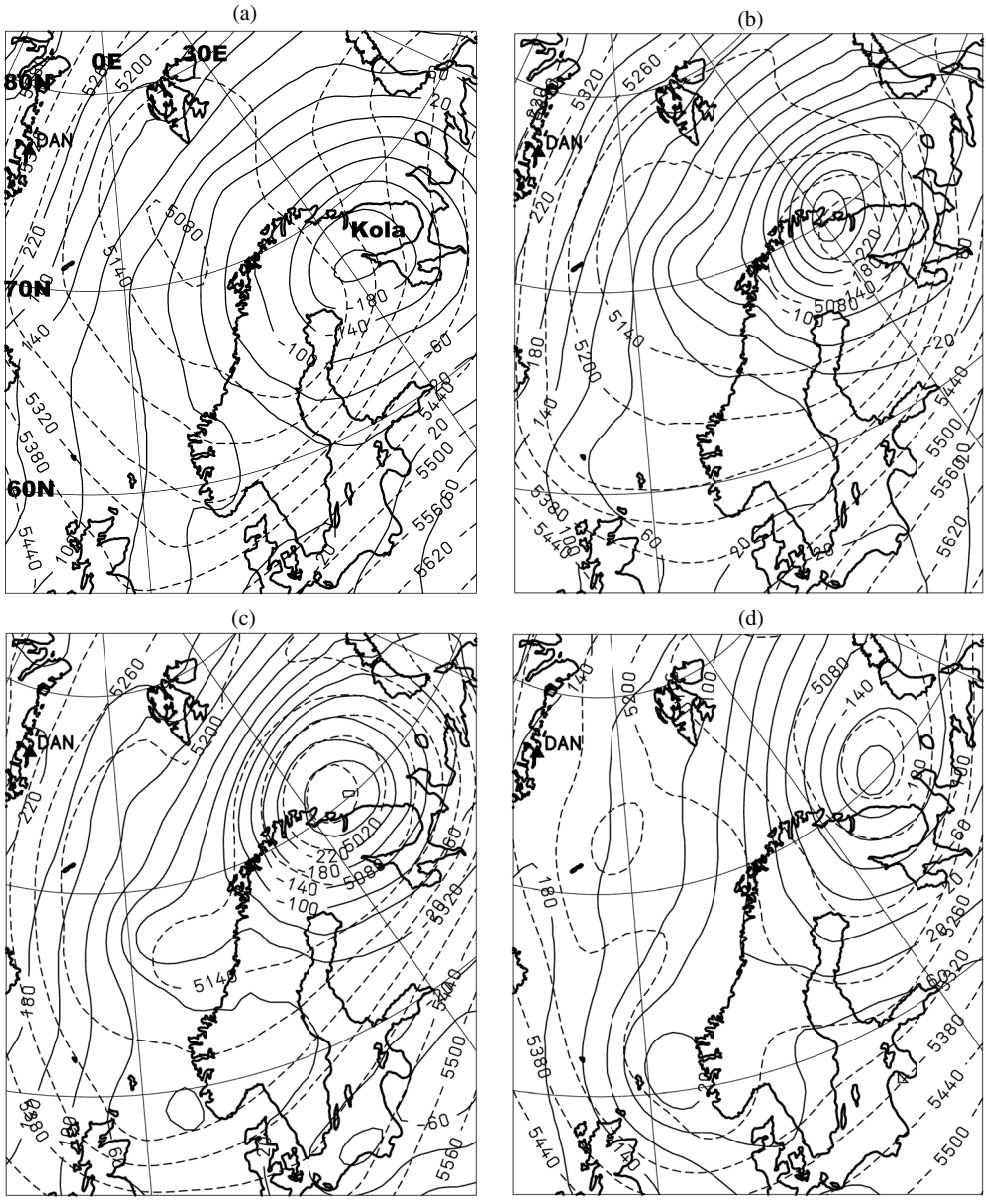

Figure 2. ECMWF analyses for the geopotential height at 1000 hPa (full lines, isolines every 40 gpm) and at 500 hPa (dashed lines, isolines every 60 gpm) for: (a) 00 UTC 14 October, (b) 12 UTC 14 October, (c) 00 UTC 15 October, and (d) 00 UTC 16 October 1993. The Kola Peninsula is marked 'Kola' in (a).

by the double peak in wind speed, the veering in wind direction and the pronounced surface pressure minimum between 03 and 06 UTC 15 October (Fig. 3). At 00 UTC on 15 October a westerly wind of almost 25 m s^{-1} is observed at the weather ship; then, from 00 until 04 UTC the pressure falls by 12 hPa, and at 06 UTC a north-easterly wind of 15 m s^{-1} is observed (Fig. 3). The AVHRR image at 1329 UTC 15 October (Fig. 1(c)) shows that the PL is associated with pronounced spiral bands. On 16 October the PL has moved to southern Norway and begins to disintegrate (Fig. 1(d)). The corresponding

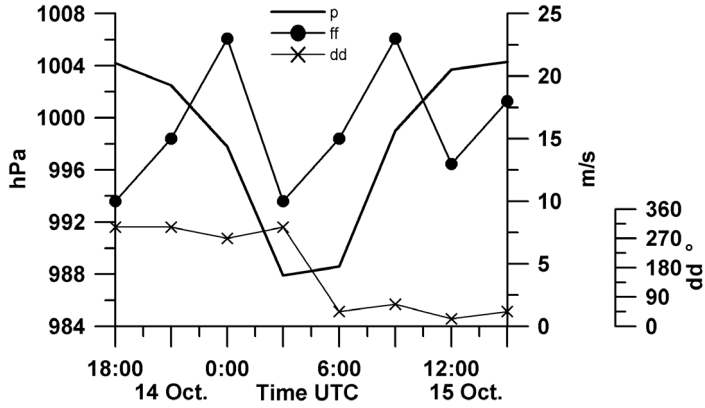

Figure 3. Pressure (bold full line), wind speed (dots) and direction (crosses) at weather ship M (position: 66°N, 2°E) from 18 UTC 14 to 15 UTC 15 October 1993.

ECMWF analysis shows the PL as a closed surface low under a broad 500 hPa trough (Fig. 2(d)).

From the satellite images (Figs. 1(b)–(d)) the changing character of the disturbance is clearly seen. The storm initially displays a distinct comma cloud signature, then develops a more spiraliform cloud pattern with embedded convective cells during its mature and decaying stages. When the disturbance crosses the south-western Norwegian coast, it dies out within a few hours.

4. Description of the evolution of the PL from satellite retrievals

(*a*) *The thermal structure*

The TOVS-derived 1000–500 hPa thicknesses (proportional to the mean temperature of this layer) valid for 13 October (at 0357 and 0541 UTC) indicate the presence of a cold air outbreak over the NWS (Fig. 4(a)). There is a strong gradient between the cold air originating from sea-ice covered areas and the warmer air to the south-east of the area. At 06 UTC 14 October the extratropical cyclone is situated at 69°N, 30°E (Berliner Wetterkarte, not shown) and the position of the corresponding warm front is such that the south-eastern part of the Barents Sea is characterized by temperatures which are much warmer than the western part. This results in a strong temperature gradient in the area between Bear Island and the north of Scandinavia, which is where the PL develops. As time passes, the 1000–500 hPa thermal field becomes more featureless in the area surrounding the PL, indicating that baroclinicity has diminished (Fig. 4(b), valid for 1341 and 1522 UTC 14 October 1993). In addition, in the formation and incipient stages of the low, the observations of 1000–850 and 850–500 hPa geopotential thicknesses (not shown) suggest high instability with cold air above relatively warm air.

The TOVS-derived TLS clearly shows the presence of a warm area corresponding to an upper-level PV anomaly to the west and the north of Scandinavia on 13 October, i.e. before the formation of the low (Fig. 5(a), valid 1353 and 1534 UTC 13 October). What is important to note is that the anomaly is situated upstream (north-west) of the developing PL, so that a positive interaction between the flow near the surface and the flow at upper levels can take place (see section 5 for a detailed discussion). Then, during its entire lifetime, an upper-level anomaly can be seen in conjunction

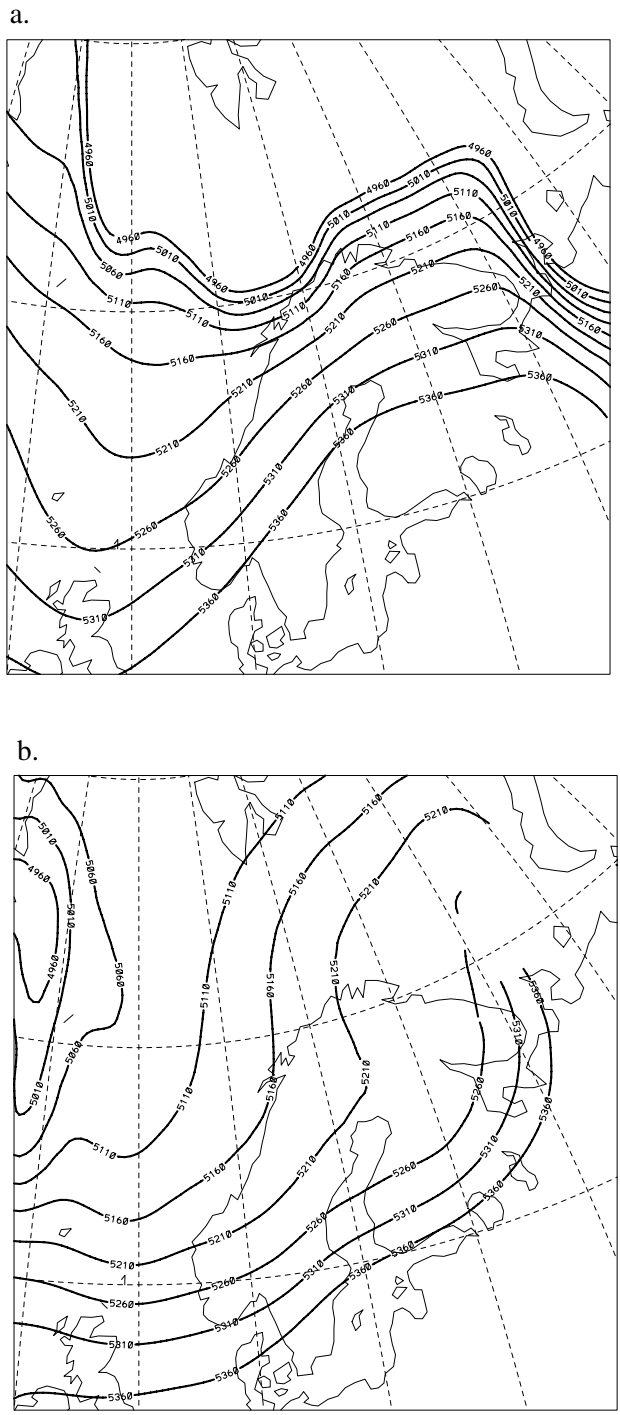

Figure 4. Geopotential thicknesses (dam, contour interval 50) between 1000 and 500 hPa retrieved from the TIROS-N Operational Vertical Sounder for: (a) 0357 and 0541 UTC 13 October, and (b) 1341 and 1522 UTC 14 October 1993.

with the surface low (Fig. 5(b), valid for 0517 and 0656 UTC 15 October), but the amplitude has diminished. At that time, there is another thermal anomaly associated with the synoptic system at 70°N, 40°E with a value of 230 K.

(*b*) *The water vapour content*

The SSM/I IWV fields for 07 UTC 14 October and 17 UTC 15 October 1993 are given in Figs. 6(a) and (b), respectively. At 07 UTC 14 October, when the PL was developing, the IWV pattern shows that the maximum water vapour content at the PL was 7.5–9 kg m^{-2}, and the values decrease to very low values of 3–4 kg m^{-2} to the north-west. This is in agreement with the thermal fields derived from TOVS, in that the PL formed at or near a boundary of dry (and cold) and moist (and warmer) air. At 17 UTC 15 October, when the PL has matured into a spiraliform shape (Fig. 1(c)), the water vapour content has a maximum value of 9–12 kg m^{-2} within the main cloudy area and the values decrease to 4–6 kg m^{-2} surrounding the PL. This increase of water vapour content within the storm as it matured could either be due to increased vertical motion and increased depth of the system, or to warming and moistening of the system over time, or to both.

(*c*) *Clouds*

In Fig. 7(a), the scattering index, S85, derived from the SSM/I is given for 12 UTC 14 October. When the values are greater than 40, this indicates the presence of large ice hydrometeors associated with convective activity. As shown in this figure, the S85 index has high values in a comma-shaped band within the developing PL, and low values associated with the synoptic system over the Barents Sea and Kola Peninsula. This means that at this early time convective processes were definitely present in the PL. When the PL reaches a mature stage (15 October) the S85 index has values below 25 within the PL (not shown), and these are too low to unambiguously conclude that significant convection is present. However, the ICLW field for this time (Fig. 7(b)) shows that the clouds are organized in spiral bands circulating around the low, and small areas within these bands have values larger than 0.2 kg m^{-2}, which are likely to be convective elements. These discrete blobs of significant ICLW contrast with the almost continuous large values of ICLW for the extratropical cyclone to the north-east.

(*d*) *Surface wind speed and sea state*

As early as 0727 UTC 14 October, wind speeds exhibit the classical couplet of low winds in the centre of the PL and strong winds to the west (Fig. 8(a)). This tendency is reinforced as time passes, with values exceeding 20 m s^{-1} on 15 October (Fig. 8(b)). These large values, in spite of possible contamination due to rather large ICLW values (Fig. 7(b)), are well corroborated by the Topex–Poseidon wind speeds derived at 0841 UTC along a north-east to south-west cross-section (Fig. 9). Wave heights of 8–9 m are associated with the largest wind speeds (Fig. 9). On 16 October, winds decreased and no longer show a distinct pattern (not shown).

Due to the Gulf Stream, the sea surface temperatures (not shown) in the vicinity of the developing low were relatively warm. The TOVS-derived thicknesses (see subsection (a)) confirm that the atmospheric boundary-layer air was quite cold. Together with the large wind speeds observed by the SSM/I (above), it is likely that turbulent fluxes of heat, moisture and momentum were large, and played an important role in the development and maintenance of the PL.

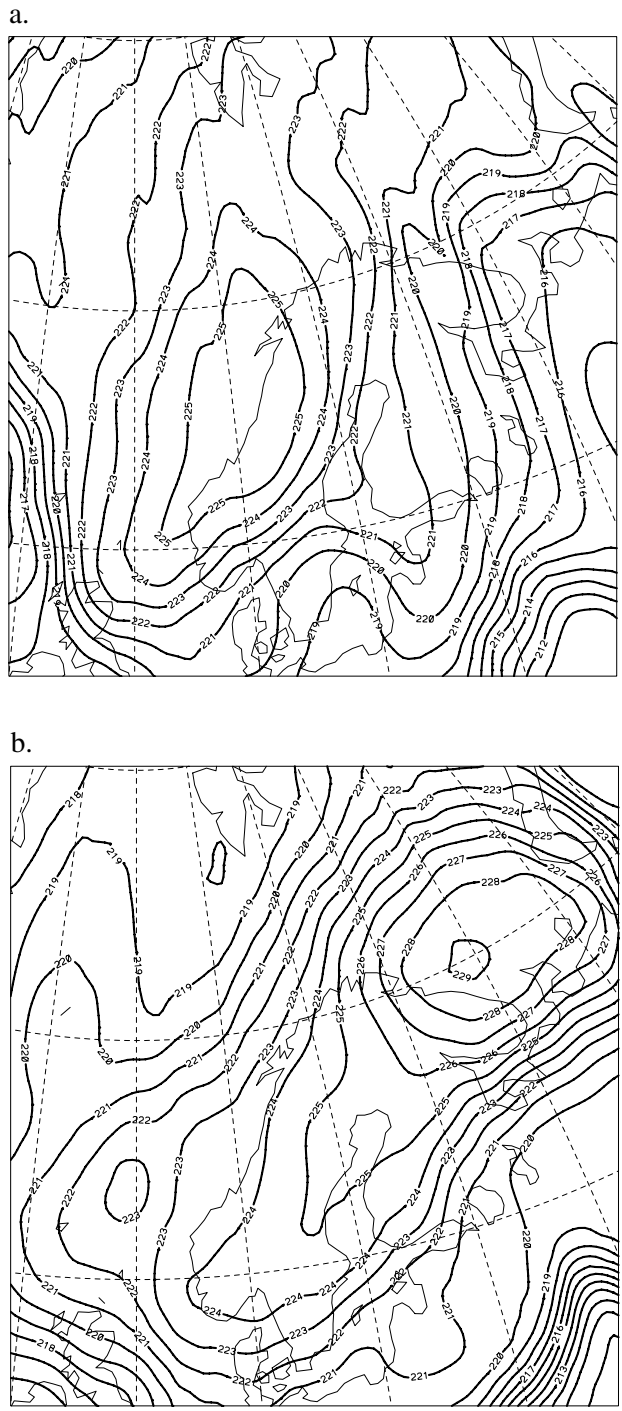

Figure 5. Temperature of the lower stratosphere (K) derived from the TIROS-N Operational Vertical Sounder for: (a) 1353 and 1534 UTC 13 October, and (b) 0517 and 0656 UTC 15 October 1993.

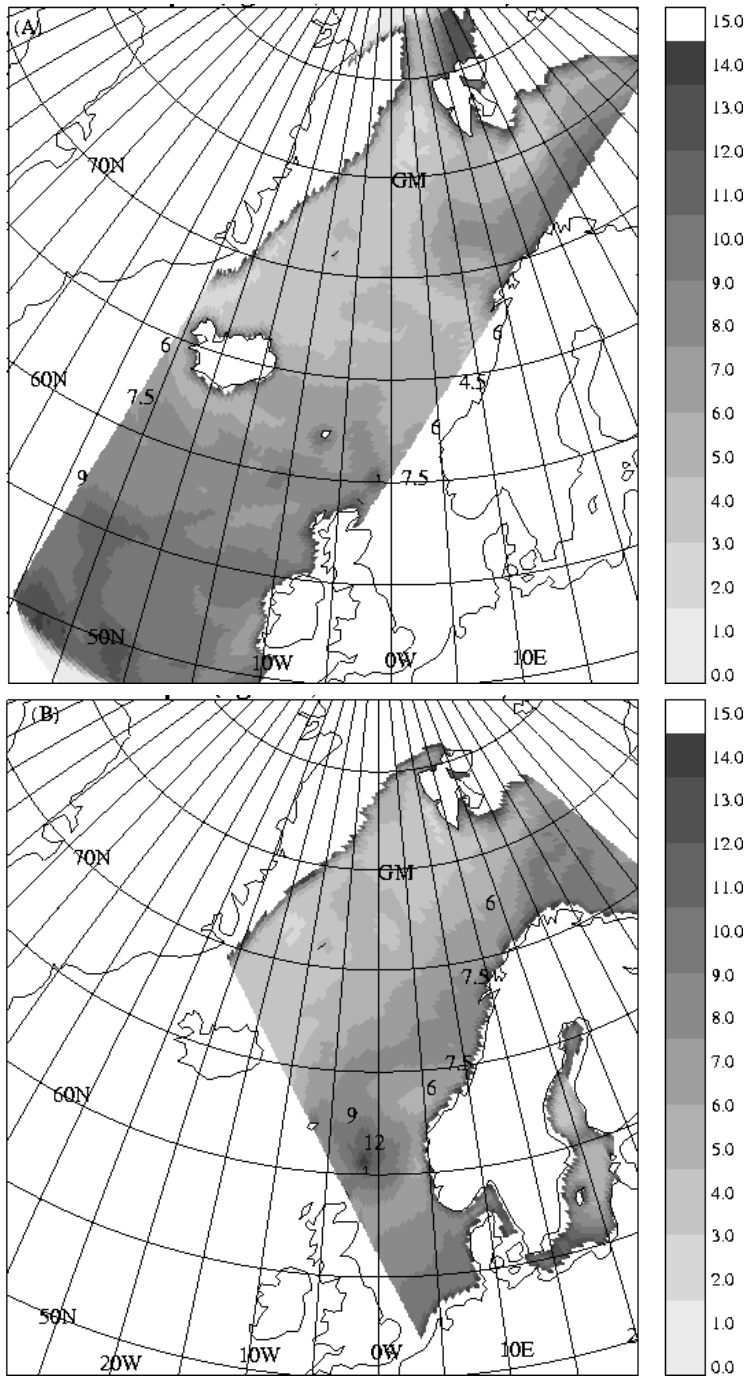

Figure 6. Integrated water vapour content (kg m^{-2}) derived from the Special Sensor Microwave/Imager for: (a) 0727 UTC 14 October, and (b) 1653 UTC 15 October 1993.

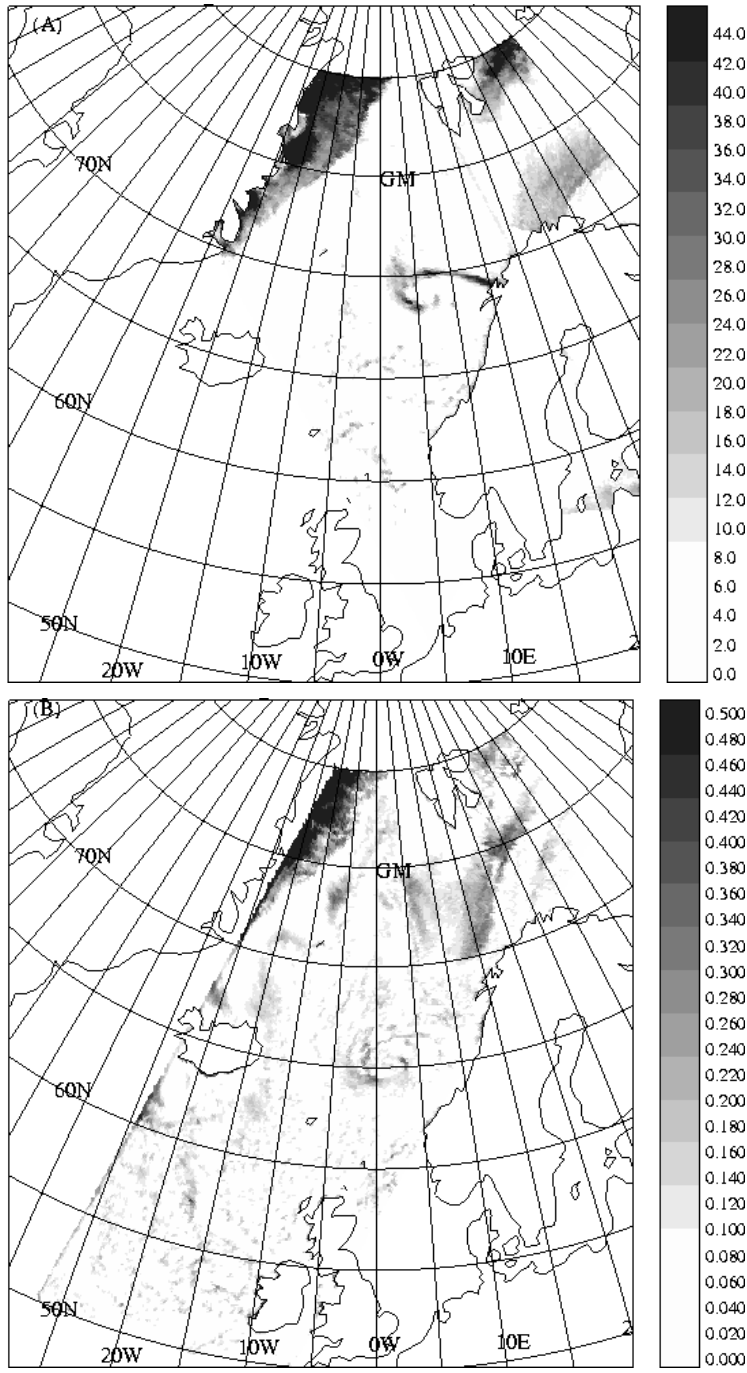

Figure 7. Retrieved Special Sensor Microwave/Imager fields over open sea: (a) 85 GHz ice scattering index (S85) for 1231 UTC 14 October, and (b) integrated cloud liquid water content (kg m^{-2}) for 0714 UTC 15 October 1993.

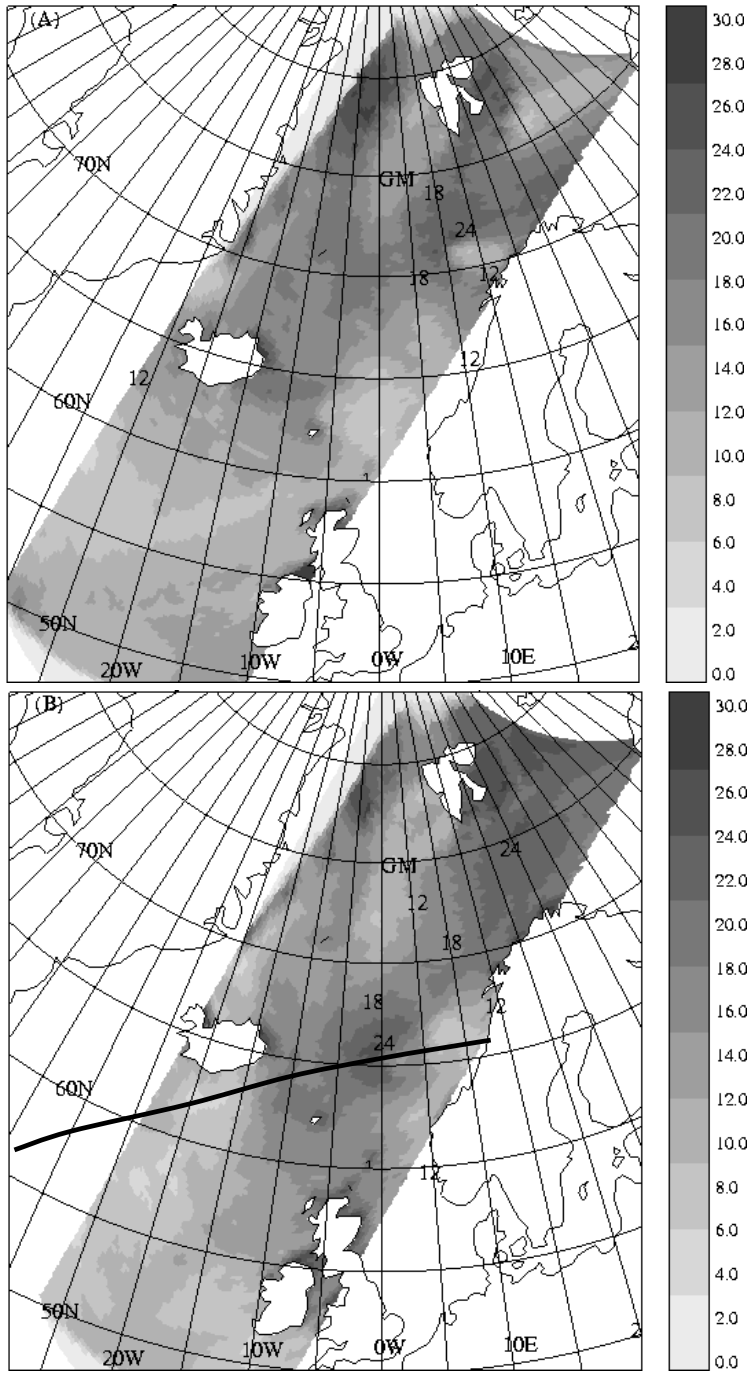

Figure 8. Surface wind speed over open sea (m s^{-1}) derived by the Special Sensor Microwave/Imager for: (a) 0727 UTC 14 October, and (b) 0714 UTC 15 October 1993. The Topex–Poseidon track from 0841 UTC 15 October 1993 is superimposed on (b) as a heavy black line.

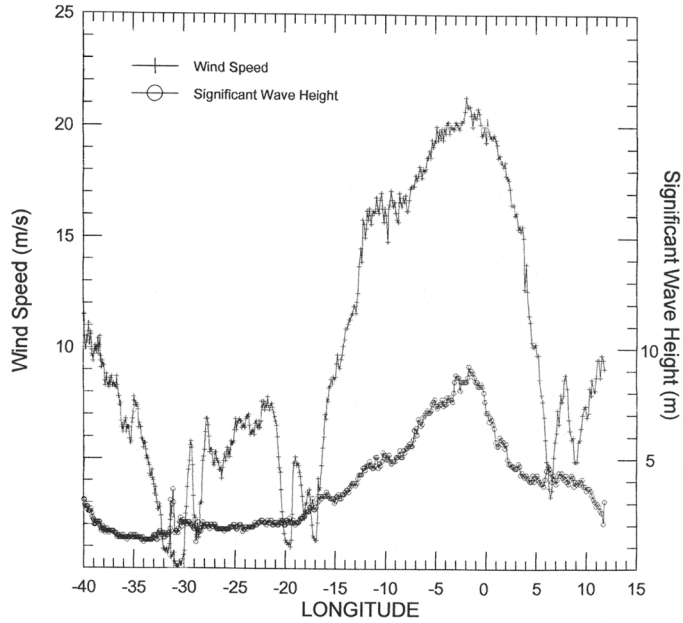

Figure 9. Topex/Poseidon-derived low-level wind speeds and significant wave height (m) for 0841 UTC 15 October 1993.

The results of the satellite-based analysis give rise to the following conclusions concerning the PL formation and development:

- its formation at the surface was very likely triggered by an upper-level PV anomaly as indicated by the TOVS-derived TLS;
- TOVS-derived thicknesses show that baroclinicity was important at the beginning of the development process, but then decreased;
- the SSM/I-derived scattering index indicates that convective processes were present in the development;
- large temperature gradients between the surface and the lowest layer of the atmosphere together with the large SSM/I-derived wind speeds indicate that turbulent fluxes at the surface might play an important role in the development and maintenance of PL.

The next step of this study consists in running limited-area models and comparing satellite retrievals with model output, in order to develop better understanding and quantification of these processes.

5. Numerical simulations of the PL development

(*a*) *IPV perspective*

(i) *Genesis stage.* The control simulation discussed here was performed using NORLAMS (see section 2), starting at 12 UTC 13 October. After 6 h of simulation (Fig. 10), a weak and warm trough has formed at low levels on the warm side of a baroclinic zone (which we identify as the Arctic front) to the east of Bear Island (B on Fig. 10). This figure shows that there is an IPV maximum of nearly 3.5 PVU* at the potential

* 1 PVU = 10^{-6} K m^{2}kg^{-1}s^{-1}.

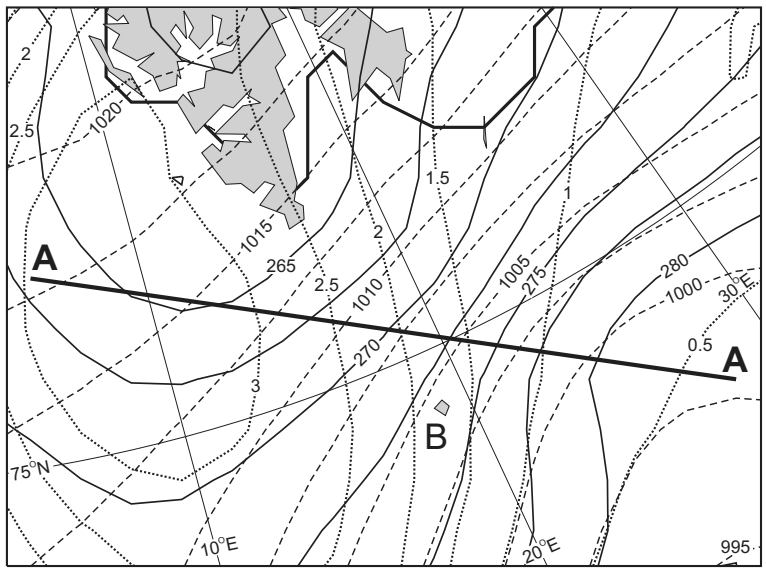

Figure 10. NORLAMS (see text) sea surface pressure (dashed lines, contour interval 2.5 hPa), equivalent potential temperature at 925 hPa (solid lines, contour interval 2.5 K), isentropic potential vorticity at $\theta = 285$ K (dotted lines, contour interval 0.5 PVU) for 18 UTC 13 October 1993. B marks the position of Bear Island. The thick solid line over the sea in the north marks surface roughness parameter = 1, which is approximately the ice edge.

temperature $\theta = 285$ K surface (pressure of about 450 hPa) to the west of the incipient surface trough. The vertical cross-section in Fig. 11 (along line AA in Fig. 10) shows that the relative vorticity maximum at 925 hPa is 1×10^{-4} s^{-1} in the trough. At this latitude the planetary vorticity f (the Coriolis parameter) is 1.4×10^{-4} s^{-1}. Figure 11 also shows that the IPV = 2 PVU surface (which we identify as the tropopause) west of the surface trough descends to around 500 hPa. Above the region of the surface trough (maximum low-level vorticity), we see from Fig. 11 that the conditional stability is marginal (equivalent potential temperature, θ_e, is nearly constant with height), and there is ascent up to above 500 hPa. The upper-level PV anomaly is in a favourable position to interact constructively with the low-level baroclinic zone so that baroclinic instability is released (that is, an upper-level positive PV anomaly lies upstream of a lower-level baroclinic zone (Hoskins *et al.* 1985; van Delden *et al.* 2003)). As a consequence, rising motion in the lower troposphere and low-level convergence take place, with resulting increased relative vorticity. This is indeed observed at later times (Figs. 12(a) and (b) after 24 h and 36 h, respectively). The relative vorticity maximum at 925 hPa has increased to 4×10^{-4} s^{-1} at 24 h, and further to 5.5×10^{-4} s^{-1} at 36 h. Since the static stability is low, the scale of the forming and developing low will be small (Montgomery and Farrell 1992).

The simulation valid at 06 UTC 14 October shows that the 500 hPa temperature is below $-42\,^{\circ}$C within a large area above and to the west of the growing surface disturbance, indicating a potentially unstable stratification in this area after 18 h of simulation (this is the case throughout the whole simulation period (not shown)). A tongue of large IPV values on the $\theta = 295$ K surface (pressure about 500 hPa) after 18 h is associated with the intrusion of cold air behind the synoptic-scale low centred (and nearly stationary) over northern Scandinavia (not shown). A region of maximum

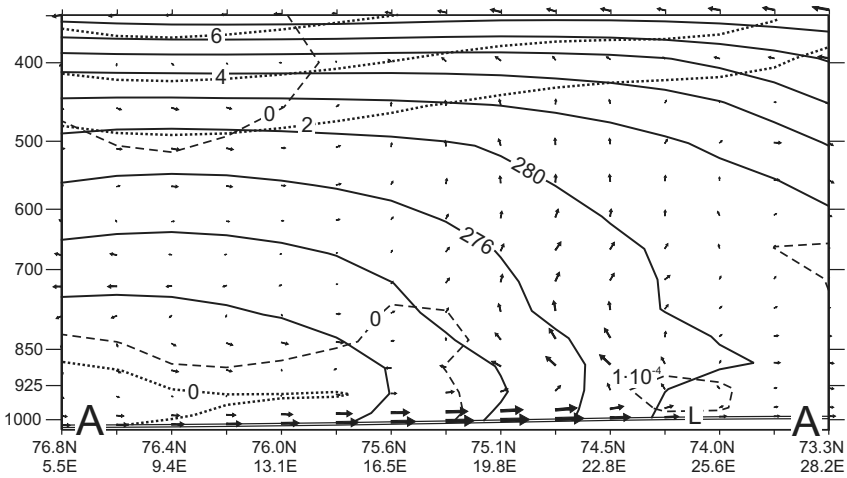

Figure 11. NORLAMS (see text) vertical cross-section along line AA in Fig. 10 for 18 UTC 13 October 1993, showing: isentropic potential vorticity (dotted lines, contour interval 2 PVU); equivalent potential temperature (solid lines; contour interval 4 K); relative vorticity (dashed lines, contour interval 10^{-4} s^{-1}). Arrows indicate ageostrophic circulation in the cross-section plane, with the length of the arrows representing displacement during 3 hours. L shows the position of the incipient surface trough.

values of IPV is centred at 72.5°N, 2°E. This IPV maximum is also evident on the $\theta = 285$ K surface at 71°N, 2°W after 24 h (Fig. 13(a)). Its position relative to the low-level trough is still favourable for the release of baroclinic instability. By 24 h the trough has developed into a closed low near the surface (Fig. 13(a)), with maximum near-surface winds well above 15 m s^{-1}, which is the lower limit for the low to be classified as a PL (Heinemann and Claud 1997; Turner *et al.* 2003).

(ii) *Mature stage.* From 24 to 36 h the PL develops further and moves south-westward at an average speed of 13 m s^{-1}. This corresponds well to the large-scale winds at 700 hPa. Since the PL moves south-westward, and the large-scale thermal wind is directed north-eastward, we have reversed-shear flow (see e.g. N97). In the simulation period from 24 to 36 h (i.e. from 12 UTC 14 to 00 UTC 15 October) the IPV maximum area (IPV $>$ 2 PVU) moves relative to the developing PL, from its western to its southern side, at the same time winding around the low, with small IPV values above the PL (Figs. 13(a) and (b)). After 36 h the interaction between the upper IPV anomaly and the surface PL is about to cease. The reason why the IPV is so small above the PL up to well above 500 hPa is that the static stability there is nearly zero.

Satellite imagery, which shows exactly the same area for about the same times (Figs. 1(b) and (c)), can be used to check the simulated position of the PL. At 12 UTC 14 October, after 24 h (Fig. 14(a)), the simulated PL is in the correct position considering that the AVHRR image is about 2 h later. The relative humidity exceeds 90% at 700 hPa, providing a good indicator of clouds at that level, and reflects well the clouds associated with the synoptic-scale cyclone over northern Norway. The axis through the relative vorticity maximum is nearly vertical after 36 h (not shown) which, from quasi-geostrophic considerations, means that the transfer from available potential energy to kinetic energy is no longer favourable. At 12 UTC 15 October, after 48 h (Fig. 14(b)), the simulated position of the PL is about 0.5 degrees too far north and 4 degrees too far west compared with the satellite imagery (Fig. 1(c)) and with the subjective analyses (albeit with only two observations in the area). However, the intensity of the PL seems

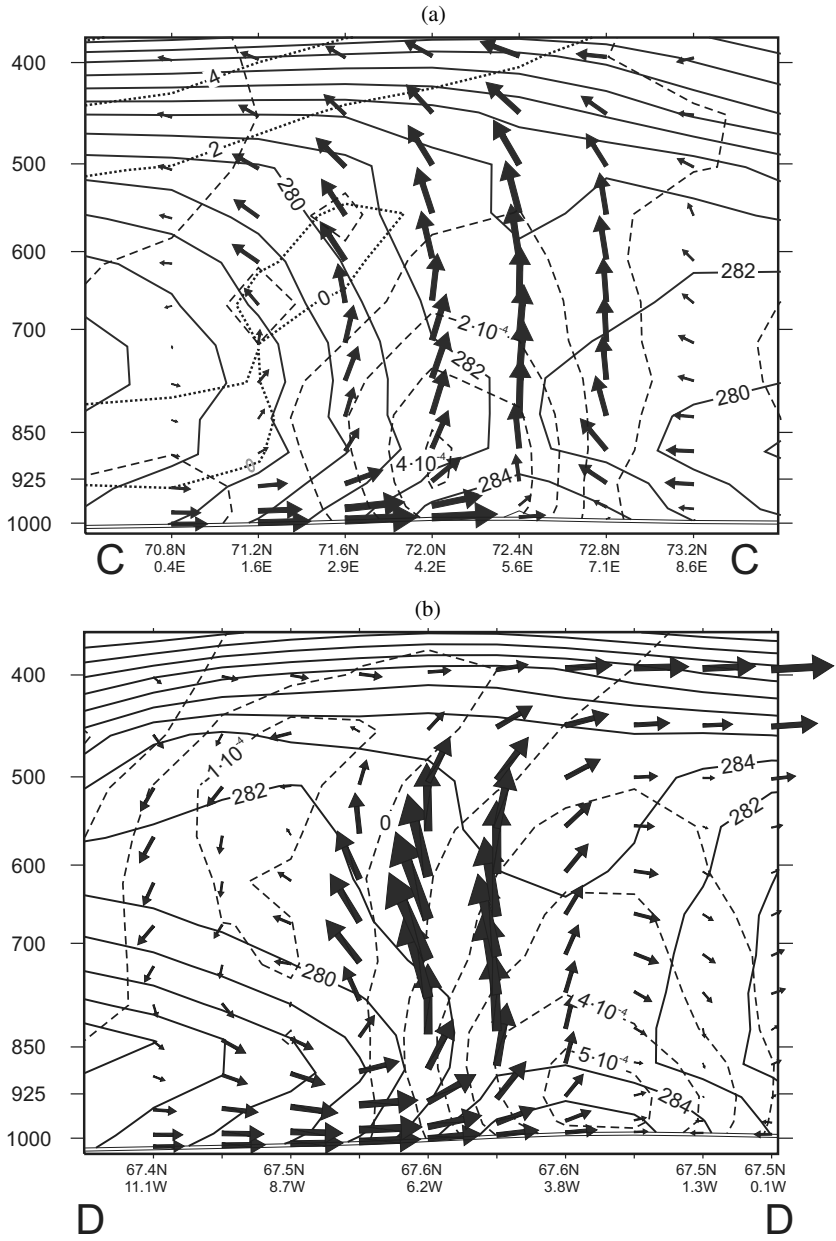

Figure 12. NORLAMS (see text) vertical cross-sections as Fig. 11 but for: (a) 12 UTC 14 October along line CC in Fig. 13(a), and (b) 00 UTC 15 October 1993 along line DD in Fig. 13(b). The equivalent potential-temperature contour interval in both (a) and (b) is 2 K, and in (b) no isentropic potential vorticity contours are given.

to be very well simulated. Since no PL was analysed in the routine analyses until 3 h earlier, we cannot compare the simulated fields at earlier times with analyses. It must be noted that N97, who initialized his simulation 12 h later, found the first signs of formation and development of a mesoscale trough 6 h into the simulation, i.e. 12 h later than in our simulation, and it was positioned further south than the position of the trough at the corresponding time in our simulation.

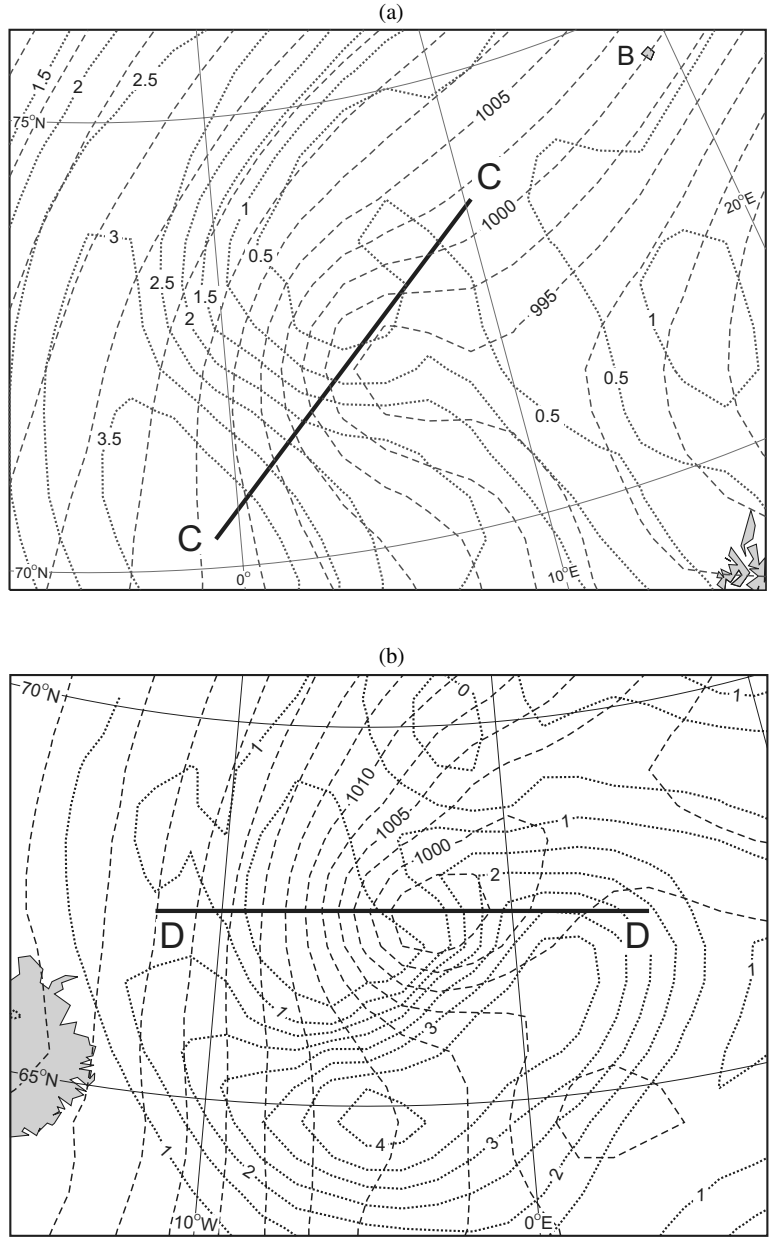

Figure 13. NORLAMS (see text) sea surface pressure (dashed lines, contour interval 2.5 hPa) and isentropic potential vorticity at potential temperature $\theta = 285$ K (dotted lines, contour interval 0.5 PVU) for: (a) 12 UTC 14 October, and (b) 00 UTC 15 October 1993.

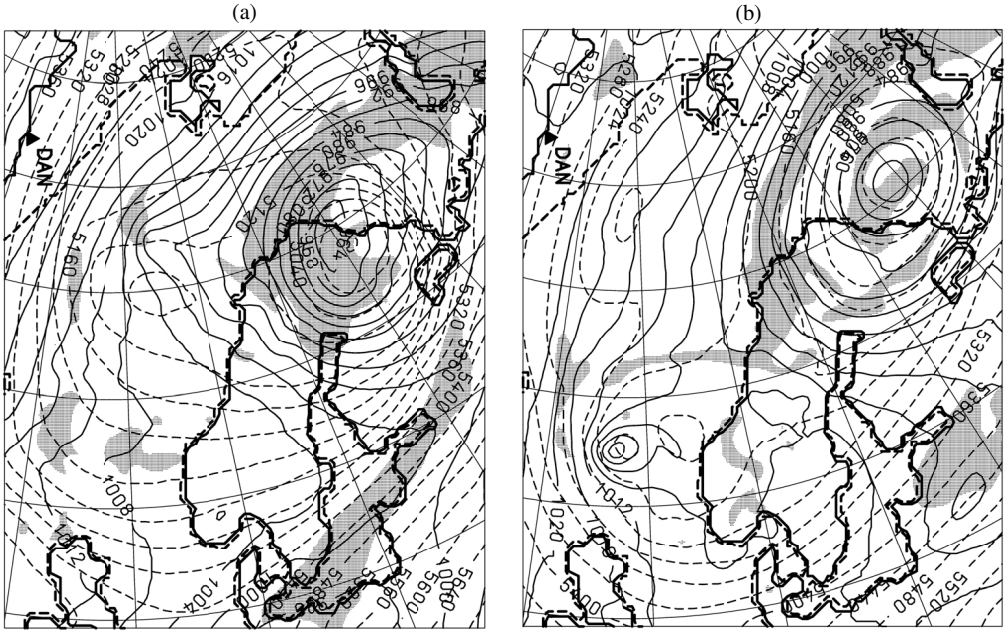

Figure 14. NORLAMS (see text) simulated mean-sea-level pressure (full lines, isolines every 4 hPa) and geopotential height at 500 hPa (dashed lines, isolines every 40 gpm) after simulation times of: (a) 24 h, valid for 12 UTC 14 October, and (b) 48 h, valid for 12 UTC 15 October 1993. Areas with relative humidity at 700 hPa exceeding 90% are shaded.

(*b*) *Dynamical processes for the PL development*

As demonstrated earlier using satellite imagery (Fig. 1) and satellite derived information (see section 4), the observed cumulus cells that grew over time illustrated that moderately strong surface sensible- and latent-heat fluxes feed the growing PL, and contribute to its extensive vertical development. This is confirmed by the control simulations, which indicate that turbulent surface fluxes of sensible and latent heat during the genesis stage (Fig. 15) are moderate and of similar magnitude, with maximum values around 325 W m^{-2} on the north western and western side of the trough, about 200 km from its centre. This is due to the strong low-level winds of 22 m s^{-1} or more.

In order to explore the role of moist processes in the development of the PL, the release of latent heat was suppressed in another simulation. Compared to the control simulation a trough formed similarly, but it did not develop beyond the stage of a moderately strong trough, far from fulfilling the criteria for a PL. So the release of latent heat due to latent-heat flux from the sea surface and horizontal convergence of water vapour from the environment played a vital role in the development from a weak trough into a strong and long-lived PL. Although the latent-heat flux off the water is important, the convergence of the moist air into the developing low and the resulting heating by condensation contributes to the formation and rapid deepening of a strong PL.

An additional numerical experiment was performed in order to assess the role of orography-induced instabilities in the formation and development of the PL. In this simulation the initial upstream topography (Novaya Zemlya, the Kola Peninsula and the Svalbard archipelago) was neglected, i.e. the height of those land surfaces was set equal to zero. In the main area of interest the results were similar to those of the control simulation. From this, we conclude that the formation of the trough is not induced by the upstream topography.

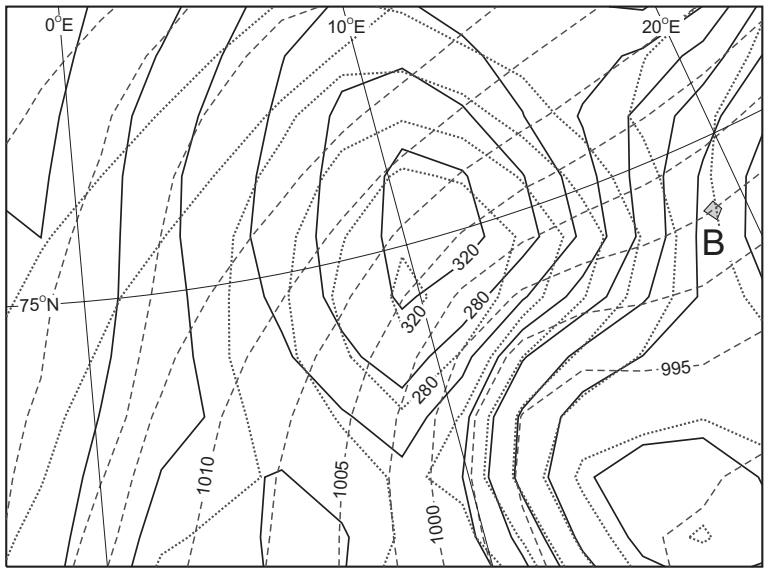

Figure 15. NORLAMS (see text) mean-sea-level pressure (dashed lines, contour interval 2.5 hPa), surface flux of sensible heat (solid lines, contour interval 40 W m^{-2}), and surface flux of latent heat (dotted lines, contour interval 40 W m^{-2}) for 06 UTC 14 October 1993.

6. Model intercomparisons and validation against satellite data

(*a*) *NORLAM/NORLAMS*

The development of the PL is described in section 5 using NORLAMS results. Although its intensification and movement is simulated quite successfully by NORLAMS over a simulation time of more than 48 h, deviations from the correct position, as detected by satellite imagery increase for longer simulation times. For a model intercomparison study, the same simulations were run using the NORLAM model. As described in subsection 2(b), both models are run under identical conditions, except for differences in the cloud parametrization schemes and resolution of the boundary layers. A comparison of both models is shown in Figs. 14 (NORLAMS) and 16 (NORLAM) for simulation times of 24 and 48 h, valid at 12 UTC 14 October and 12 UTC 15 October, respectively. During the first 24 h, the differences between the two model runs in terms of the surface pressure and upper-level geopotential are relatively small (Figs. 14(a) and 16(a)). However, the simulated mid-level clouds (i.e. areas with a relative humidity larger than 90% at 700 hPa) of the NORLAM simulation are in better agreement with the observed cloud structure on the satellite image than the NORLAMS run, suggesting the importance of the vertical resolution. At 24 h simulation time, the NORLAM humidity field reflects *le Cygne* structure as seen in Fig. 1(b). Larger differences between NORLAM and NORLAMS fields are found for 48 h simulation time (Figs. 14(b) and 16(b)). Both models simulate the southward movement of the PL, but NORLAM places the PL centre more to the east and with a deeper central pressure. The analysis of the MSLP at 00 UTC 16 October shown by N97 yields a central pressure of 995 hPa and a position of 61°N, 2°E. The 60 h NORLAM simulation also valid at 00 UTC 16 October (not shown) shows the PL at exactly the same position with a central pressure of 996 hPa. Therefore, the NORLAMS simulation (Fig. 14(b)) underestimates the eastward movement and the deepening of the PL in its mature phase. The NORLAM

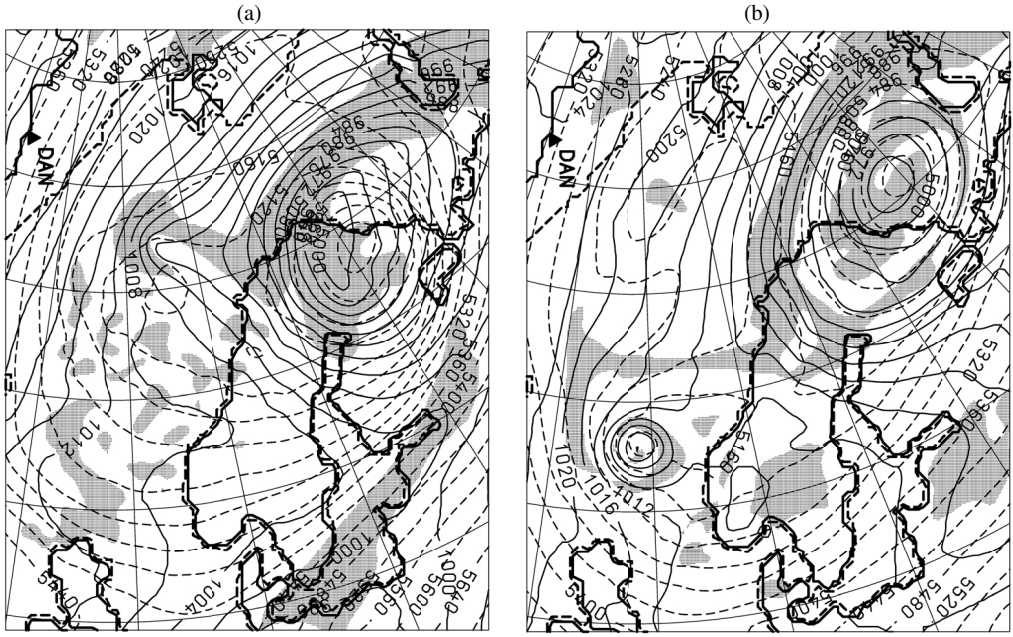

Figure 16. As Fig. 14, but for the NORLAM (see text) simulation.

humidity field after 48 h (Fig. 16(b)) also shows well the spiral structure around the PL centre.

(*b*) *Comparisons of model simulations and satellite retrievals*

Since model and satellite retrievals are at about the same spatial resolution, it is of interest to compare numerical outputs to the satellite (TOVS and SSMI) retrievals for validation purposes. NORLAM simulations are used in this section, since their agreement with the satellite imagery observations was better for simulation times exceeding 36 h compared to NORLAMS.

For temperature fields, comparisons are concentrated on the layer 1000–500 hPa and they are performed over sea and land; for humidity (IWV) and near-surface wind speeds, which are retrieved from SSM/I, comparisons are restricted to areas of open sea. While TOVS radiances are part of the ECMWF data assimilation system, the SSM/I retrievals and Topex–Poseidon-retrieved surface winds represent independent data of relatively good accuracy, which can be used to monitor the model forecast quality (see Lieder and Heinemann 1999).

(i) *Temperature fields.* On 13 October, in both the satellite retrievals and the model, the cold air outbreak is well observed, leading to strong gradients from the North Sea to the Gulf of Bothnia and farther over the Barents Sea (not shown). A fair quantitative agreement is also observed. On the morning of 14 October there is good overall qualitative agreement between the observations and the simulated fields, with the model thicknesses on average larger than TOVS. On the evening of 14 October, rejections in the TOVS retrievals associated with the extratropical cyclone, due to rain over the Barents Sea, preclude comparisons over this area; elsewhere, there is again good agreement between the two fields (Figs. 17(a) and 4(b)). On the next day, both in the morning and

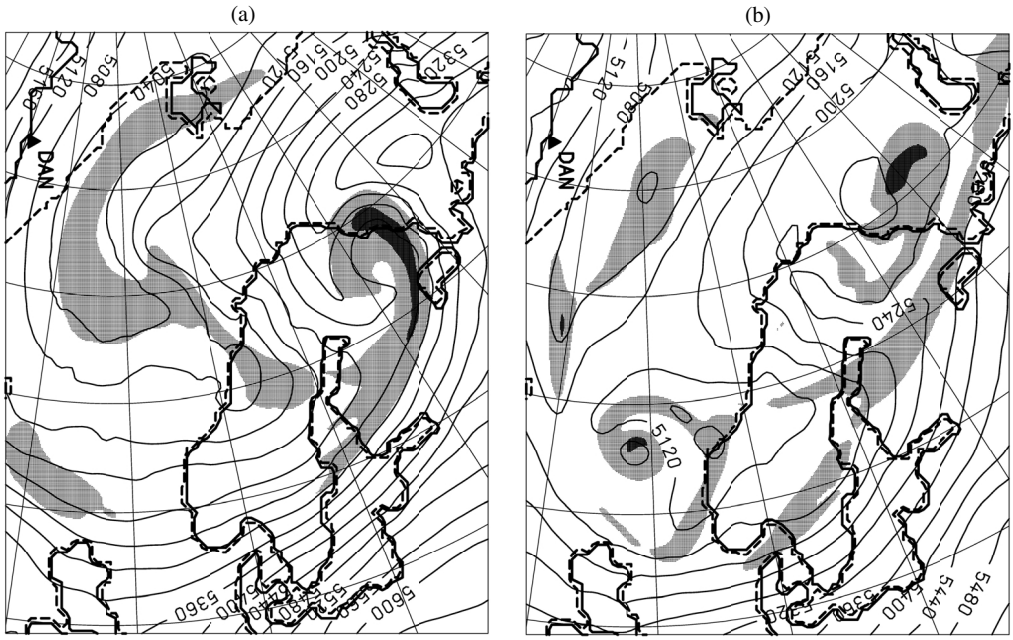

Figure 17. NORLAM (see text) 500–1000 hPa thickness (isolines every 40 dam), and potential vorticity at 500 hPa (values larger than 1.5 PVU with light shading, values larger than 3.5 PVU with dark shading) for simulation times of: (a) 24 h, valid for 12 UTC 14 October, and (b) 48 h, valid for 12 UTC 15 October 1993.

in the evening, the model, due to its finer resolution, provides more detail in the structure about the PL itself (colder air in the area corresponding to the centre and warmer air to the west, well corroborated by satellite humidity fields), but once again the large-scale features are in good agreement. On 16 October in the decaying stage of the PL similar remarks are still valid.

Comparisons for the layers 1000–850 and 500–300 hPa (not shown) lead to the same conclusions:

- a good agreement for large-scale features, with satellite retrievals generally biased low compared to the model outputs;
- more mesoscale structures for the PL itself in model simulations, due to the finer spatial resolution (25 versus 100 km).

The TLS, which represents the mean temperature of a layer situated above the tropopause, cannot directly be compared to any model field; however, a correlation is found between the position of warm TLS values and that of high 500 hPa PV values simulated by both models. The correlation is better as time goes by (Figs. 17(b) and 5(b)), very likely because at the beginning of the period TLS sounds an area which is situated higher than 500 hPa. This is corroborated by the fact that at 12 UTC 13 October, there is a good agreement between the potential temperature at 300 hPa (not shown), with a maximum value of 318 K which corresponds to a real temperature of 225 K, and the TLS maximum.

(ii) *Humidity fields.* NORLAM-simulated humidity and near-surface wind fields are provided in Figs. 18(a) and (b) for 06 UTC and 18 UTC 15 October, respectively. In the incipient stage of the PL, simulated IWV fields (not shown) are less organized than SSM/I retrievals in the area where the PL forms. Significant differences appear,

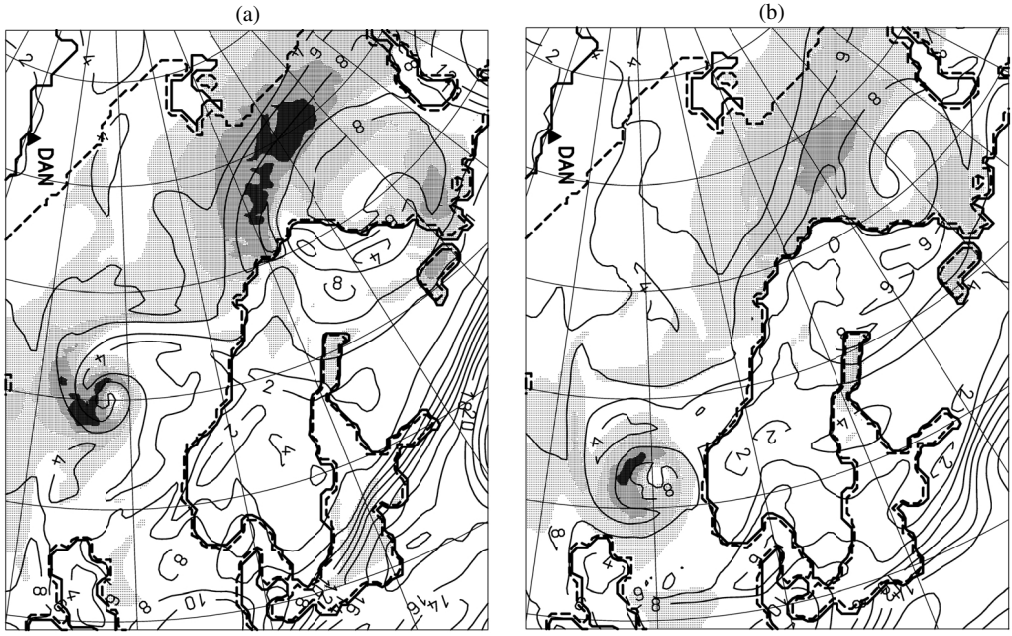

Figure 18. NORLAM-simulated (see text) integrated water vapour (isolines every 2 kg m^{-2}) and 10 m wind (shaded for wind speeds exceeding 10 m s^{-1} with shading increment 4 m s^{-1}) for simulation times of: (a) 42 h, valid for 06 UTC 15 October, and (b) 54 h, valid for 18 UTC 15 October 1993.

especially in the Barents Sea north of Finland where the model simulates large water vapour amounts compared to SSM/I. But gradually the model produces smaller amounts of water vapour over this area, leading to a better overall agreement. A better agreement is found in the PL area during the mature phase, the model reproducing clearly the region of moist air isolated from the surroundings; simulated IWV values are, however, smaller than observed values (18 UTC 15 October, Figs. 18(b) and 6(b)).

(iii) *Near-surface wind fields.* As expected, the NORLAM model produces somewhat less structure than SSM/I, but the classical couplet of low winds in the centre of the PL and larger wind speeds to the south-west is clearly simulated; however, in the incipient stage of the PL gradients are less steep than in satellite retrievals. Modelled wind speeds larger than 20 m s^{-1} are in good agreement with SSM/I and Topex–Poseidon-retrieved values to the west of the mature low, and in the Barents Sea in connection with the synoptic-scale low (Figs. 18(a) and 8(b)).

7. Discussion and conclusions

A long-lasting PL (three days) has been investigated using satellite observations and model simulations. In this study observations from four different sensors have been used, namely an imager, a vertical sounder, a microwave passive sensor and a microwave active sensor. At the time of the PL, the ERS-1 satellite carrying the first satellite-borne C-band scatterometer was already launched. Unfortunately, there were no good scatterometer data during the period of interest. From these other instruments temperature and humidity fields, as well as information on clouds (integrated cloud liquid water content and presence of large ice particles), surface wind speeds and sea state can be derived.

The analysis of all satellite-derived fields has led to the following conclusions concerning the PL:

- its formation was very likely triggered by an upper-level anomaly;
- baroclinicity was important at the beginning of the development process, but decreased later;
- convective processes were present in the PL;
- large temperature gradients between the surface (Gulf Stream) and the lowest layer of the atmosphere, together with the large wind speeds, indicate that fluxes were certainly important in the development and maintenance of the PL.

In a next step, in order to verify these hypotheses and better quantify all these processes, two limited-area models have been run (NORLAMS as used at the University of Bergen, and NORLAM version 9 as used at Meteorologisches Institut Universität Bonn (MIUB)). In addition, at the University of Bergen different experiments have been conducted for isolating other probable causes of development. A validation of the simulations has been performed by comparing the model outputs and the satellite retrievals. The comparisons showed that both models provided good simulations of the PL, with the essential features clearly reproduced. Both models are initialized by ECMWF analyses which in the subsequent operational ECMWF forecasts indicate only the development of a weak trough, while the mesoscale models simulate the PL well with a pressure anomaly of about 16–20 hPa. As expected, the quality (position and intensity of the low) decreases with increasing forecast time, but it has also been observed that the resolution of the boundary layer (number of levels in the lowest 1–2 km) alone modified the movement of the disturbance in the simulations. For simulation times exceeding 36 h, despite having the less advanced scheme for cloud liquid water, the NORLAM model simulates the movement of the PL better than NORLAMS. From these simulations we can conclude that the number of vertical levels in the lower 2 km is an important ingredient for the simulation of the trajectory of this low. In addition, in spite of a better spatial resolution, humidity and surface wind speeds are generally slightly less organized in the simulations than in SSM/I retrievals. This illustrates the importance of considering model simulations in conjunction with satellite observations to obtain a very complete description and understanding of PLs.

The results presented here are in good agreement with those of N97 for the developed and mature phases of the low; he proposed an explanation of the development based on the generalized forms of the equations for omega and geopotential tendency. However, for the early stages of development, a powerful insight into the origins and development is given by the so-called IPV thinking. In our opinion *le Cygne* PL was the result of favourable flow conditions at the surface, in the form of a shallow Arctic front established south of the ice edge, together with an upper-level PV anomaly upstream, setting the stage for a positive interaction. Their subsequent interaction explains why the developing low-level wave propagates southwards, from near the ice edge zone into the NWS. As the IPV anomaly moves south, a phase-locking between the growing surface disturbance and upper IPV anomaly occurs. Later on, the moderately strong surface sensible- and latent-heat fluxes (influence of the large wind speeds and the Gulf Stream) plus the horizontal convergence of humid air toward the PL contributed to the extensive vertical development.

ACKNOWLEDGEMENTS

We are grateful to E. Rasmussen who drew our attention to this PL and to N. W. Nielsen for fruitful scientific discussions. Thanks are due to the members of ARA/LMD

group for the processing of TOVS data, and to N. Mognard for the processing of TOPEX/POSEIDON data. We acknowledge the contributions of T. Klein and M. Lieder, who performed the NORLAM runs and the AVHRR processing at MIUB, respectively. Thanks also to F. Cleveland for assistance with editing the figures of section 5.

References

Businger, S. and Reed, R. J. 1989 Polar lows. Pp. 3–45 in *Polar and arctic lows*. Eds. P. F. Twitchell, E. A. Rasmussen and K. L. Davidson. A. Deepak Publishing, Virginia, USA

Carleton, A. M., McMurdie, L. A., Katsaros, K. B., Zhao, H., Mognard, N. M. and Claud, C. 1995 Satellite-derived features and associated atmospheric environments of southern ocean mesocyclone events. *The Global Atmos. and Ocean System*, **3,** 209–248

Chedin, A., Scott, N. A., Wahiche, C. and Moulinier, P. 1985 The improved initialization inversion: A high resolution physical method for temperature retrievals from satellites of the TIROS-N series. *J. Clim. Appl. Meteorol.*, **24,** 124–143

Claud, C., Scott, N. A., Chedin, A. and Gascard, J. C. 1991 Assessment of the accuracy of atmospheric temperature profiles retrieved from TOVS observations by the 3I method in the European Arctic: Application for mesoscale weather analysis. *J. Geophys. Res.*, **96,** 2875–2887

Claud, C., Mognard, N. M., Katsaros, K. B., Chedin, A. and Scott, N. 1993 Satellite observations of a polar low over the Norwegian Sea by Special Sensor Microwave/Imager, Geosat and TIROS-N Operational Vertical Sounder. *J. Geophys. Res.*, **98,** 14487–14506

Emanuel, K. A. 1986 An air–sea interaction theory for tropical cyclones. Part I: Steady-state maintenance. *J. Atmos. Sci*., **43,** 585–604

Emanuel, K. A. and Rotunno, R. 1989 Polar lows as arctic hurricanes. *Tellus*, **41A,** 1–17

Fourrié, N., Claud, C., Donadille, J., Cammas, J. P., Pouponneau, B. and Scott, N. A. 2000 The use of TOVS observations for the identification of tropopause-level thermal anomalies. *Q. J. R. Meteorol. Soc*., **126,** 1473–1494

Goodberlet, M. A., Swift, C. T. and Wilderson, J. C. 1989 Remote sensing of ocean surface winds with the Special Sensor Microwave/Imager. *J. Geophys. Res.*, **94,** 14547–14555

Grønås, S., Foss, A. and Lystad, M. 1987 Numerical simulations of polar lows over the Norwegian Sea. *Tellus*, **39A,** 334–353

Heinemann, G. 1996 A wintertime polar low over the eastern Weddel Sea (Antarctica): A case study with AVHRR, TOVS, SSM/I and conventional data. *Meteorol. Atmos. Phys*., **58,** 83–102

1998 A meso-scale model-based study of the dynamics of a wintertime polar low in the Weddell Sea region of the Antarctic during WWSP86. *J. Geophys. Res.*, **103,** 5983–6000

Heinemann, G. and Claud, C. 1997 Report of a workshop on 'Theoretical and observational studies of polar lows' of the European Geophysical Society Polar Lows Working Group. *Bull. Am. Meteorol. Soc.*, **78**(11)**,** 2643–2658

Heinemann, G., Noel, S., Chedin, A., Scott, N. A. and Claud, C. 1995 Sensitivity studies of TOVS retrievals with 3I and ITPP retrieval algorithms: Application to the resolution of mesoscale phenomena in the Antarctic. *Meteorol. Atmos. Phys.*, **55,** 87–100

Hewson, T. D., Craig, G. C. and Claud, C. 2000 Evolution and mesoscale structure of a polar low outbreak. *Q. J. R. Meteorol. Soc*., **126,** 1031–1063

Hollinger, J., Lo, R., Poe, G., Savage, R. and Pierce, J. 1987 'Special Sensor Microwave/Imager User's Guide'. Naval Research Laboratory, Washington, DC, USA

Hoskins, B. J., McIntyre, M. E. and Robertson, A. W. 1985 On the use and significance of isentropic potential vorticity maps. *Q. J. R. Meteorol. Soc*., **111,** 877–946

Joly, A., Jorgensen, D., Shapiro, M. A., Thorpe, A. J., Bessemoulin, P., Browning, K. A., Cammas, J. P., Chalon, J. P., Clough, S. A., Emanuel, K. A., Eymard, L., Gall, R., Hildebrand, P. H., Langland, R. H., Lemaitre, Y., Lynch, P., Moore, J. A., Persson, P. O. G., Snyder, C. and Wakimoto, R. M. 1997 The Fronts and Atlantic Storm-Track Experiment (FASTEX): Scientific objectives and experimental design, *Bull. Am. Meteorol. Soc*., **78**(9)**,** 1917–1940

Klein, T. and Heinemann, G. 2002 Interaction of katabatic winds and mesocyclones at the eastern coast of Greenland. *Meteorol. Appl.*, **9,** 407–422

Köpken, C., Heinemann, G., Chedin, A., Claud, C. and Scott, N. A. 1995 Assessment of the quality of TOVS-retrievals obtained with the 3I algorithm for Antarctic conditions. *J. Geophys. Res.*, **100,** 5143–5158

Kvamstø, N. G. 1992 'Implementing the Sundqvist Scheme in the Norwegian Limited Area Model'. Met. Report Series 2. Available from Department of Meteorology, Geophysical Institute, University of Bergen, Norway

Lieder, M. and Heinemann, G. 1999 A summertime Antarctic mesocyclone over the southern Pacific during FROST SOP 3: A meso-scale analysis using AVHRR, SSM/I, ERS and numerical model data, *Weather and Forecasting*, **14,** 893–908

McMurdie, L. A., Claud, C. and Atakturk, S. 1997 Satellite-derived characteristics of spiral and comma-shaped southern hemisphere mesocyclones. *J. Geophys. Res.*, **102,** 13889–13905

Montgomery, M. T. and Farrell, B. F. 1992 Polar low dynamics. *J. Atmos. Sci*., **49,** 2484–2505

Nielsen, N. W. 1997 An early autumn polar low formation over the Norwegian Sea. *J. Geophys. Res.*, **102,** 13955–13973

Nordeng, T. E. 1990 A model-based diagnostic study of the development and maintenance mechanism of two polar lows. *Tellus*, **42A,** 92–108

Nordeng, T. E. and Rasmussen, E. A. 1992 A most beautiful polar low: A case study of a polar low development in the Bear Island region. *Tellus*, **44A,** 81–99

Petty, G. W. 1994a Physical retrievals of over-ocean rain rate from mutichannel microwave imagery. Part 1: Theoretical characteristics of normalized polarization and scattering indices. *Meteorol. Atmos. Phys.*, **54,** 79–100

1994b Physical retrievals of over-ocean rain rate from mutichannel microwave imagery. Part 2: Algorithm implementation. *Meteorol. Atmos. Phys.*, **54,** 101–122

Rasmussen, E. A. 1989 A comparative study of tropical cyclones and polar lows. In *Polar and arctic lows.* Eds. P. F. Twitchell, E. A. Rasmussen and K. L. Davidson. A. Deepak Publishing, Virginia, USA

Rasmussen, E. A., Claud, C. and Purdom, J. F. 1996 Labrador Sea polar lows. *The Global Atmos. and Ocean System*, **4,** 275–333

Scott, N. A., Chedin, A., Armante, R. A., Francis, J., Stubenrauch, C., Chaboureau, J. P., Chevallier, F., Claud, C. and Cheruy, F. 1999 Characteristics of the TOVS Pathfinder Path-B dataset. *Bull. Am. Meteorol. Soc*., **80,** 2679–2701

Smith, W. L., Woolf, H. M., Hayden, C. M., Wark, D. Q. and McMillin, L. M. 1979 The TIROS-N Operational Vertical Sounder. *Bull. Am. Meteorol. Soc.*, **60**(10)**,** 1177–1187

Sundqvist, H., Berge, E. and Kristjansson, J. E. 1989 Condensation and cloud parameterization studies with a mesoscale numerical weather prediction model. *Mon. Weather Rev*., **117,** 1641–1657

Turner, J., Rasmussen, E. A. and Carleton, A. M. 2003 Introduction. In *Polar lows.* Eds. E. A. Rasmussen and J. Turner. Cambridge University Press, Cambridge, UK

Van Delden, A., Rasmussen, E. A., Turner, J. and Røsting, B. 2003 Theoretical Investigations. In *Polar lows.* Eds. E. A. Rasmussen and J. Turner. Cambridge University Press, Cambridge, UK

Witter, D. L., and Chelton, D. B. 1991 A Geosat altimeter wind speed algorithm development, *J. Geophys. Res.*, **96,** 8853–8860